SACLANT UNDERSEA RESEARCH CENTRE REPORT

FINITE DIFFERENCE MODELLING OF SCATTERING BY OBJECTS IN THE SEABED

J.A. Fawcett and J.L.T. Grimbergen

July 1996
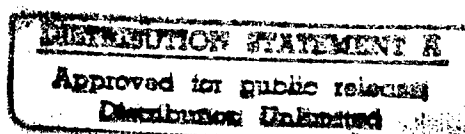
DTIC QUALITY INSPECTED 4

19961203 018

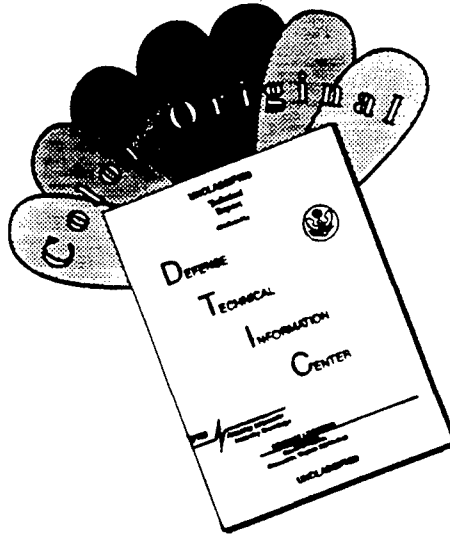NATO SACLANT Undersea Research Centre
Viale San Bartolomeo 400
19138 San Bartolomeo (SP), Italy

Tel: +39 187 540.111
Fax: +39 187 524.600

e-mail: library@saclantc.nato.int

NORTH ATLANTIC TREATY ORGANIZATION

DISCLAIMER NOTICE
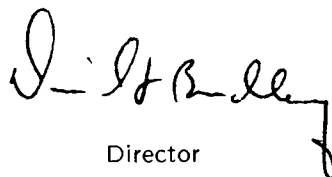
THIS DOCUMENT IS BEST QUALITY AVAILABLE. THE COPY FURNISHED TO DTIC CONTAINED A SIGNIFICANT NUMBER OF COLOR PAGES WHICH DO NOT REPRODUCE LEGIBLY ON BLACK AND WHITE MICROFICHE.

Finite Difference Modelling of
Scattering by Objects in the Seabed

John A. Fawcett and
Joris L.T. Grimbergen

The content of this document pertains to
work performed under Project 033-3 of
the SACLANTCEN Programme of Work.
The document has been approved for
release by The Director, SACLANTCEN.

Director

intentionally blank page

Finite Difference Modelling of Scattering by Objects in the Seabed

John A. Fawcett and Joris L.T. Grimbergen

Executive Summary:

A better understanding of the scattering of acoustic energy from elastic objects on or under the seabed will lead to a significant improvement in our ability to detect and classify minelike objects. Modelling of such scattering should include the effects of the seabed itself since mines may be buried to some degree. The Finite Difference method, described in this report, allows acoustic scattering from mines in complex bathymetric conditions to be modelled. This gives insight into the physical mechanisms and environmental parameters which are important to the scattering of energy from mines and will act as a benchmark for faster, but more approximate, models.

This report describes some of the theory and implementation issues concerned with Finite Difference modelling. For an illustration of the value of this method, the results of computations of scattering from buried and partially buried cylinders for smooth and rough seabed conditions are presented. Numerical examples are also given, illustrating the accuracy of the method for problems, such as scattering from aluminum cylinders, where analytic solutions are known. It is clear many questions regarding the effects of burial and bathymetry on mine scattering are answered by the FD model.

intentionally blank page

     NATO UNCLASSIFIED

Finite Difference Modelling of
Scattering by Objects in the Seabed

John A. Fawcett and Joris L.T. Grimbergen

Abstract: In this report we describe the theory and some implementation issues of a finite difference code used at SACLANT Centre. In particular, we consider the modelling of attenuation and the excitation of a remote incident field by using Huygen's sources. A series of comparisons of finite difference results with analytical results is performed. The report concludes with a series of computations of scattering of a generalized plane wave from a buried cylinder where the transmitted portion of the generalized plane wave is evanescent. An example of time-reversed propagation of a scattered field is also given.

Keywords: Finite difference modelling, attenuation, Huygen's sources

Joris L.T. Grimbergen is now with Shell International Exploration and Production, Research and Technical Services (SIEP/RTS), Volmerlaan 8, 2288 GD Rijwijk, The Netherlands.

Contents

1

Introduction

Finite Difference (FD) modelling can compute the time-domain solution to complex elastic scattering problems (for example, [1, 2, 3, 4]). The FD solutions include all angles of energy propagation - both forward and backward propagating energy. The method is very general in terms of the environment and the scattering objects and surfaces. There is no need to make assumptions about range-independence, the shapes of objects, etc. The chief disadvantage of the method is that it becomes computationally intensive for grid sizes which are more than 100 wavelengths in a dimension (for three-dimensional modelling this problem is even more acute). Thus for problems where the source of incident energy is distant from the scattering region it is not possible to model the source region. In order to resolve this shortcoming, we have implemented a technique for bringing remote incident fields into the numerical grid. This means that in the case where a large portion of the waveguide is simple in structure, we can model the propagation of the incident field up to the boundary of the grid with a more efficient technique. Similarly, once the scattered field has been computed by the FD method, it should be possible to extrapolate the scattered field to remote receivers.

In the Spring of 1995, SACLANTCEN obtained the visco-elastic finite difference code developed by J. Robertsson, J. Blanch, and W. Symes [5, 6]. This method includes additional variables and parameters which allow for the modelling of spatially-varying compressional and shear attenuations. We shall refer to this code as the RBS code for the remainder of this report. We implemented the basic code into a MATLAB [7] package for FD modelling. This package provides subroutines for the construction of the fields required by the FD code. This includes the construction of stress and strain relaxation time grids for desired Q (the number of wavelengths over which the amplitude decays by $e^{-\pi}$) grids for the compressional and shear waves. It also includes a subroutine for the analytic computation of the generalized plane-wave incident field along a boundary of the finite difference grid for a 2 half-space environment. The incident field, in this case, consists of a coherent sum of direct, reflected, and transmitted components. This field is used to excite sources along this boundary in the FD computations, effectively bringing the incident field into the grid. The FD code is fourth-order accurate spatially and uses a staggered grid formulation [4]. It is second order in time. In many instances, 20 grid points *per* wavelength give very good results with this code (for a broadband source, this corresponds to fewer points *per* wavelength for frequencies higher than the centre

value).

Below, we will describe in more detail some of the features of the FD code; in particular, we will describe some of the details of the attenuation modelling, the boundary absorbing layer, and the incident field modelling. We will then present the results from a sequence of benchmark computations which test the attenuation and the elastic scattering capabilities of the code. In order to reduce computation time, the numerical examples of this report were run using a FORTRAN implementation of the code rather than the MATLAB package.

2

Theory

In this section we describe some of the theoretical and implementation issues connected with the visco-elastic finite difference modelling.

2.1 The basic model

The basic set of visco-elastic differential equations solved by the RBS code is

$$
\begin{aligned}
\frac{\partial \sigma_{xx}}{\partial t} &= \eta \frac{\tau_\epsilon^p}{\tau_\sigma}\left(\frac{\partial v_x}{\partial x} + \frac{\partial v_z}{\partial z}\right) - 2\mu \frac{\tau_\epsilon^s}{\tau_\sigma}\frac{\partial v_z}{\partial z} + r_{xx} \\
\frac{\partial \sigma_{xz}}{\partial t} &= \mu \frac{\tau_\epsilon^s}{\tau_\sigma}\left(\frac{\partial v_x}{\partial z} + \frac{\partial v_z}{\partial x}\right) + r_{xz} \\
\frac{\partial \sigma_{zz}}{\partial t} &= \eta \frac{\tau_\epsilon^p}{\tau_\sigma}\left(\frac{\partial v_x}{\partial x} + \frac{\partial v_z}{\partial z}\right) - 2\mu \frac{\tau_\epsilon^s}{\tau_\sigma}\frac{\partial v_x}{\partial x} + r_{zz} \\
\frac{\partial v_x}{\partial t} &= \frac{1}{\rho}\left(\frac{\partial \sigma_{xx}}{\partial x} + \frac{\partial \sigma_{xz}}{\partial z}\right) \\
\frac{\partial v_z}{\partial t} &= \frac{1}{\rho}\left(\frac{\partial \sigma_{xz}}{\partial x} + \frac{\partial \sigma_{zz}}{\partial z}\right) \\
\frac{\partial r_{xx}}{\partial t} &= -\frac{1}{\tau_\sigma}\left(r_{xx} + \eta\left(\frac{\tau_\epsilon^p}{\tau_\sigma} - 1\right)\left(\frac{\partial v_x}{\partial x} + \frac{\partial v_z}{\partial z}\right) - 2\mu\left(\frac{\tau_\epsilon^s}{\tau_\sigma} - 1\right)\frac{\partial v_z}{\partial z}\right) \\
\frac{\partial r_{zz}}{\partial t} &= -\frac{1}{\tau_\sigma}\left(r_{zz} + \eta\left(\frac{\tau_\epsilon^p}{\tau_\sigma} - 1\right)\left(\frac{\partial v_x}{\partial x} + \frac{\partial v_z}{\partial z}\right) - 2\mu\left(\frac{\tau_\epsilon^s}{\tau_\sigma} - 1\right)\frac{\partial v_x}{\partial x}\right) \\
\frac{\partial r_{xz}}{\partial t} &= -\frac{1}{\tau_\sigma}\left(r_{xz} + \mu\left(\frac{\tau_\epsilon^s}{\tau_\sigma} - 1\right)\left(\frac{\partial v_x}{\partial z} + \frac{\partial v_z}{\partial x}\right)\right)
\end{aligned}
$$

(1)

where σ_{ij} denotes the components of the symmetric stress tensor, v_i is the velocity vector, μ is the shear relaxation modulus, and η is the compressional relaxation modulus, corresponding to $\lambda + 2\mu$ in the standard elastic problem. The variables r_{ij} are memory variables [8] which are introduced for the visco-elastic modelling in order to avoid the explicit computation of time-convolution terms. For the simple attenuation model considered in this report, three memory variables are required. Associated with the attenuation modelling are the parameters τ_ϵ^p, the compressional strain relaxation time, τ_ϵ^s, the shear strain relaxation time, and τ_σ the stress relaxation time which for our model is the same for compressional and shear waves. In the limit of no attenuation, $\tau_\epsilon^p/\tau_\sigma$ and $\tau_\epsilon^s/\tau_\sigma$ become unity and r_{ij} becomes zero.

The above equations then reduce to the standard equations of elasticity. In the following subsection, we discuss in more detail the modelling of attenuation.

As with all FD codes the differential equations are discretized in both space and time to yield a set of discrete equations. The RBS code uses a discretization of Eq.(1) which is fourth order accurate in space and second order in time. In order to obtain accurate answers using the FD code we find in practice that we require 10-20 spatial grid points for the dominant wavelength of the problem. This criterion is dependent upon the frequency bandwidth of the source; if, for example, there is significant energy at frequencies twice the main frequency, these wavelengths must also be accurately modelled. The required spatial discretization of a wavelength indicates the problem which arises when dealing with low-velocity zones; the wavelengths are small in these regions and hence these zones require a small spatial step. The code of this report uses uniform spacing, so that, in fact, a small spacing must be used for the entire grid in this case. These low velocity cases may arise when we wish to model an object filled with air ($c_p \approx 340 m/s$) or when we wish to accurately model the effects of shear. Shear velocities may often be only a few hundred m/s.

The RBS is an explicit FD code and hence the time step Δt must satisfy a constraint of the form $\Delta t \leq \alpha \Delta x / c_{max}$ where Δx is the spatial step size if the solution is to be stable with respect to time. This has two main implications for the modelling; (1) if one decreases the spatial grid size, then it is necessary to decrease the time step accordingly (2) a zone of high velocity will require small time steps and since the time step is the same for the entire grid, this may force the time step to be inordinately small in other regions of the grid. For the RBS code the maximum value of α is approximately 0.606 [9].

2.2 Attenuation Modelling

We will give a brief outline of the theory of visco-elastic modelling to give an understanding of some of the parameters and implementation issues involved. Here, we follow the notation of the appendix in [6]. The constitutive relation for a visco-elastic medium can be modelled as being time-dependent,

$$\sigma_{ij} = \dot{\Lambda} * \epsilon_{kk}\delta_{ij} + 2\dot{M} * \epsilon_{ij} \tag{2}$$

where σ_{ij} is the stress tensor of Eqs.(1), ϵ_{ij} is the strain tensor, Λ and M correspond to the Lamé constants λ and μ, and δ_{ij} denotes the Kronecker delta. Equation (2) can be rewritten in terms of compressional Γ and shear parameters M as

$$\sigma_{ij} = (\dot{\Gamma} - 2\dot{M}) * \epsilon_{kk}\delta_{ij} + 2\dot{M} * \epsilon_{ij}. \tag{3}$$

The form of Eqs.(2) and (3) is similar to the standard constitutive relations except that now the parameters Λ, Γ, and M are time-dependent and multiplications have

become time-convolutions. A useful model for the time history of Γ and M is

$$\Gamma(t) = \Gamma_R\left[1 - \sum_{\ell=1}^{L}\left(1 - \frac{\tau_{\epsilon\ell}^p}{\tau_{\sigma\ell}}\right)e^{-t/\tau_{\sigma\ell}}\right]U(t) \tag{4}$$

and

$$M(t) = M_R\left[1 - \sum_{\ell=1}^{L}\left(1 - \frac{\tau_{\epsilon\ell}^s}{\tau_{\sigma\ell}}\right)e^{-t/\tau_{\sigma\ell}}\right]U(t) \tag{5}$$

where $U(t)$ is Heaviside's function, $\tau_{\epsilon\ell}^p$ and $\tau_{\epsilon\ell}^s$ are the compressional and shear strain relaxation times for the ℓ'th term in Eqs.(4-5), and $\tau_{\sigma\ell}$ are the corresponding stress relaxation times. Following [6] we have chosen the parameters $\tau_{\sigma\ell}$ to be the same for both the compressional and shear functions and hence we do not use a superscript for this parameter. In the frequency domain the complex compressional and shear moduli are given by

$$\tilde{\Gamma}(\omega) = F\left[\frac{d}{dt}(U(t)\Gamma(t))\right] \tag{6}$$

$$\tilde{M}(\omega) = F\left[\frac{d}{dt}(U(t)M(t))\right] \tag{7}$$

where F denotes the Fourier Transform. In order to simplify our analysis we will consider $\ell = 1$ in Eqs. (4-5) and will no longer use the subscript ℓ in our notation. We will consider only the compressional term $\tilde{\Gamma}(\omega)$. The analysis of the shear function proceeds along identical lines. Using Eq.(4) in Eq.(6) yields

$$\tilde{\Gamma}(\omega) = \frac{1 + i\omega\tau_\epsilon}{1 + i\omega\tau_\sigma}. \tag{8}$$

In terms of $\tilde{\Gamma}(\omega)$ the quality factor Q can be written

$$Q(\omega) \equiv \frac{\Re[\tilde{\Gamma}(\omega)]}{\Im[\tilde{\Gamma}(\omega)]} = \frac{1 + \omega^2\tau_\epsilon\tau_\sigma}{\omega(\tau_\epsilon - \tau_\sigma)}. \tag{9}$$

where $\Re$ and $\Im$ denote the real and imaginary parts of a complex number respectively. This factor is the number of wavelengths a harmonic plane-wave must propagate before its amplitude has been decreased by a factor of $\exp(-\pi)$. The phase velocity $c(\omega)$ for each Fourier component of the wavefield can also be computed from $\tilde{\Gamma}(\omega)$ and is given by

$$c^2(\omega) = \frac{\tau_\epsilon}{\tau_\sigma}\frac{M_R}{\rho}\left\{1 + \left[\frac{\tau_\epsilon}{\tau_\sigma} - 1\right]\frac{1}{1 + \omega^2\tau_\epsilon^2}\right\}^{-1}. \tag{10}$$

From Eq.(10) it can be seen that there is frequency dispersion in this visco-elastic medium. In order to have a causal system it is, in fact, necessary to have some frequency dispersion[10].

Introducing

$$\tau_\gamma \equiv \frac{\tau_\epsilon}{\tau_\sigma} - 1 \tag{11}$$

into Eq.(9), we can write

$$Q^{-1}(\omega) = \frac{\omega \tau_\sigma \tau_\gamma}{1 + \omega^2 \tau_\sigma^2 (1 + \tau_\gamma)}. \tag{12}$$

For reasonable values of Q, $\tau_\gamma \ll 1$ and hence

$$Q^{-1}(\omega) \approx \frac{\omega \tau_\sigma \tau_\gamma}{1 + \omega^2 \tau_\sigma^2}. \tag{13}$$

In order to determine optimal values of τ_σ and τ_γ to approximate a constant Q over a given frequency band, [6] gives a simple, but effective algorithm based upon Eq.(13). Basically τ_γ controls the amplitude of $Q^{-1}(\omega)$ and τ_σ controls the frequency offset of the curve. The parameter τ_σ is set to $1/(2\pi f_c)$ where f_c is the centre frequency of the frequency interval of interest and τ_γ is determined by a simple linear optimization algorithm.

The same type of algorithm can also be used in the case of more than one (i.e., $\ell > 1$ in Eq.(4)) attenuation mechanism: $\tau_{\sigma,\ell}$ are set for specified frequencies over the bandwidth and a value of τ_γ is determined to yield a good approximation to constant Q over the entire frequency band. By taking several attenuation mechanisms, it is possible to obtain an excellent approximation to a constant Q. In the numerical code of this report only one mechanism is used. Although this does not model a constant Q over the entire band of interest, we will see in the numerical examples that, in practice, it does a good job in modelling the attenuation and dispersion effects of visco-elasticity.

In Fig. 1 we plot Eq.(9) as a function of frequency. We have determined the optimal values of τ_γ for the frequency interval [100,3000] Hz for constant Q values of 20 (which corresponds to 1.36 dB/λ) and 50 (which corresponds to 0.54 dB/λ). The Q for the single mechanism model is approximately constant in the interval [750,3000] Hz. For frequencies higher or lower than these values, the Q values produced by the model are too high. If the frequency content of the source is concentrated in the interval where the constant Q approximation is good, then we expect the single-mechanism Q model to be effective.

In Fig. 2 we show the velocity/frequency curve computed from Eq.(10) for the computed values of τ_σ and τ_γ for the $Q = 20$ (solid) and $Q = 50$ (dashed) cases. The phase velocity varies from about 1500 m/s at f=300 Hz to 1575 m/s at f=5000 Hz for the $Q = 20$ case and the variation is almost linear between 500 and 1500 Hz. The velocity variation is much less for the $Q = 50$ case; there is only a variation of 30 m/s over the entire frequency range.

Based on the theoretical analysis of Futterman [11] and the experimental work of Wuenschel [12], the following Q/dispersion model for real visco-elastic materials has
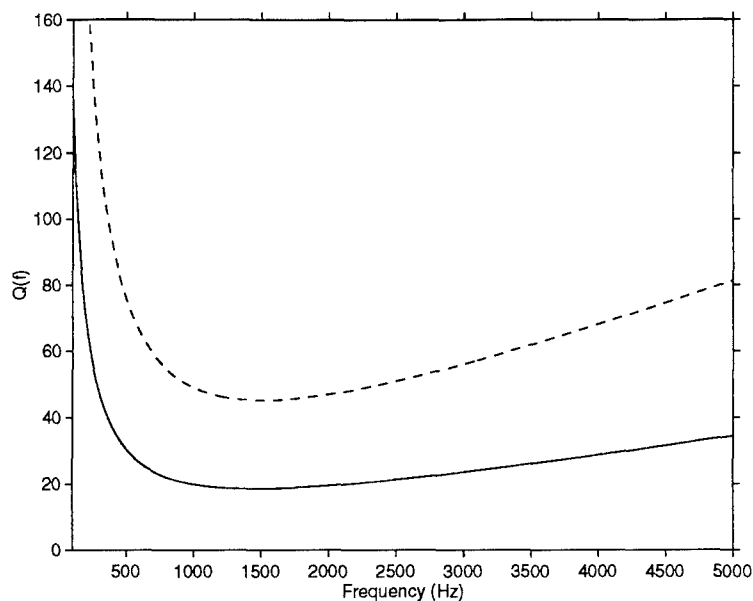
Figure 1: *Computed Q as a function of frequency, approximating Q=20 (solid line), Q=50 (dashed line)*

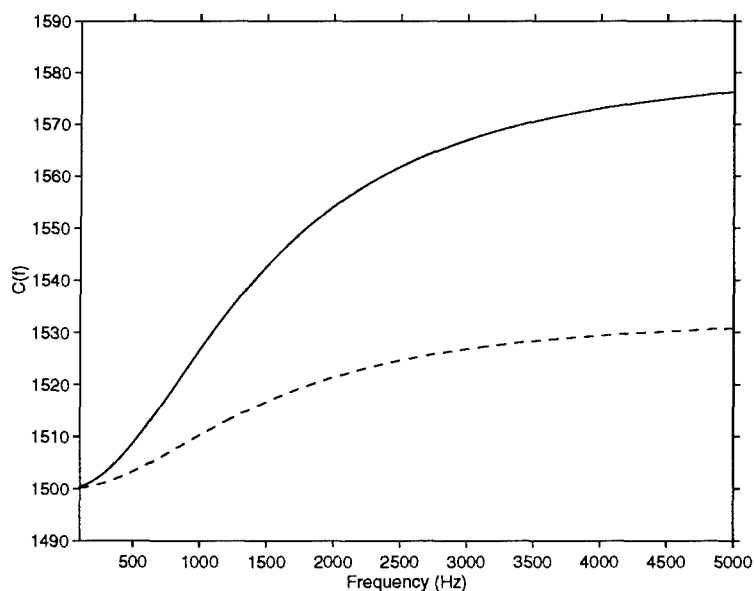

Figure 2: *Computed phase velocity as a function of frequency for modelled Q=20 (solid line), Q=50 (dashed line)*

been suggested

$$c(\omega) = c_0\left[1 - \frac{1}{2\pi Q_0}ln|(\omega/\omega_0)^2 - 1|\right]^{-1} \tag{14}$$

$$Q(\omega) = Q_0\left[1 - \frac{1}{2\pi Q_0}ln|(\omega/\omega_0)^2 - 1|\right]. \tag{15}$$

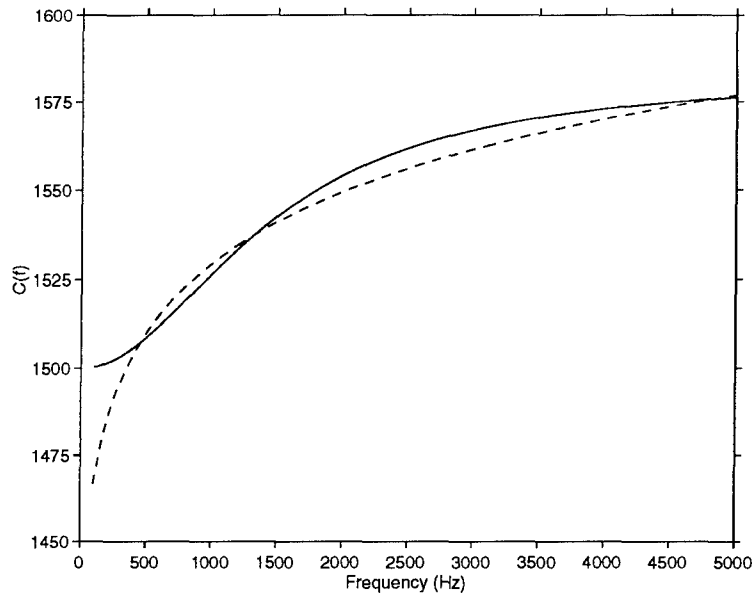There are three parameters in Eqs. (14) and (15) to choose, namely ω_0, c_0 and

Figure 3: *Computed phase velocity as a function of frequency for Q=20 using Eq. (10) (solid line) and Eq. (14) (dashed line)*

Q_0. The parameter ω_0 is a frequency taken to be well below the frequency band of interest, c_0 is a velocity chosen to yield a desired phase velocity at a specific frequency and Q_0 is some constant Q-value. In Figs. 3 and 4 we show the curves computed from Eqs. (14) and (15) with the corresponding curves for $Q(\omega)$ and $c(\omega)$ in Figs.1 and 2 for a value of $Q = 20$. We have used $Q_0 = 20$, $\omega_0 = 0.1Hz$, and c_0 is chosen such that $c(200Hz) = 1485m/s$ in Eq. (14) and (15).

From Fig. 3 we can see that with the appropriate choice of parameters the curve computed from Eq. (14) agrees well with the curve computed for the single-mechanism model except at the low frequencies. The value of $Q(\omega)$ computed from Eq. (15) is essentially constant, with a value slightly less than 20, over the frequency range shown.

We have analyzed the characteristics of the single-mechanism model in the frequency domain. However, the Finite Difference code is implemented in the time domain. From Eq. (3) this would seem to require the computation of time-convolution terms
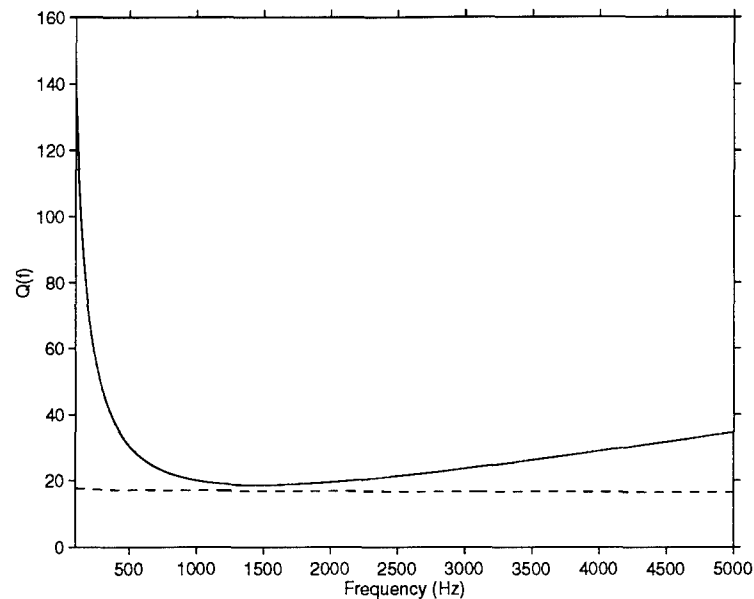
Figure 4: *Computed Q as a function of frequency for Q=20 using Eq.(9) (solid line) and Eq.(15) (dashed line)*

at each spatial grid point. Fortunately, due to the form of $\Gamma(t)$ and $M(t)$ in Eqs. (4) and (5) each of the convolution expressions for σ_{xx}, σ_{zz} and σ_{zx} can be expressed in terms of a time-dependent term and time-dependent variables r_{xx}, r_{zz} and r_{xz} respectively which satisfy straightforward differential equations. Thus, instead of explicitly computing time convolutions, the differential equations for the convolutions are updated at the same time steps as the standard, elastic differential equations. For the single-mechanism model, three extra differential equations are required (at each spatial point).

In the MATLAB implementation of the code, a module has been written which takes user-specified grids of Q-values and sound speeds and converts this into grids of τ_ϵ and τ_σ values. These grids are required by the FD code for the attenuation modelling.

2.3 Boundary attenuation

In order to make the computational grid for the FD method finite, it is necessary to impose some boundary conditions on the elastic field at finite values of x and z. The true boundary conditions are that the scattered portions of the field should be only outgoing and it is possible to simulate these boundary conditions with varying degrees of accuracy [13]. The approach of the FD code of this report is to set the elastic variables to zero at the edges of the grid. This causes a spurious reflection

of energy incident on the sides of the grid. In order to eliminate this artificially reflected energy, an attenuating layer is introduced to the grid, running parallel to the sides of the grid. Two MATLAB modules have been written for the creation of this attenuating layer. The first module follows the suggestion of [5] and allows the user to define a very low Q value at the edge of the grid (e.g. $Q = 2$). A smooth transition from the true Q-value in the interior of the grid to the low value at the edge is used (typically, a transition over 20-40 grid points is used). Thus we are applying the visco-elastic capabilities of the code to the problems of artificial reflections from the grid boundaries. As was explained in the previous subsection (see Fig.2) there is significant dispersion for low values of Q. In order to eliminate reflections caused by the change of phase velocity due to changing Q, the compressional and shear velocities defined on the grid are adjusted using Eq.(10) so that the phase velocity at the dominant frequency of the problem is a constant with respect to Q. Automatic velocity-tuning is a feature of the MATLAB module. A second
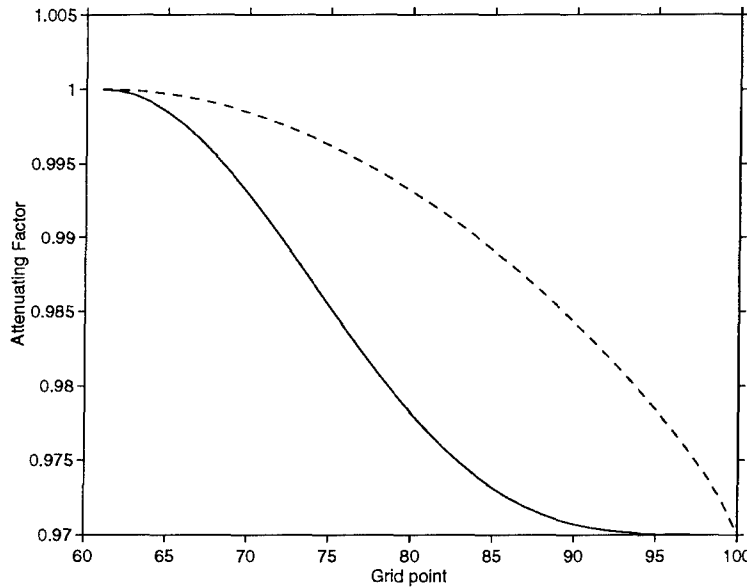

Figure 5: *Attenuating factor from Eq.(16) for a transition layer of 40 grid points using p=2 (solid line) and p=0.4 (dashed line).*

attenuation mechanism is implemented by multiplying the wavefield within the attenuating layer solution by a constant ζ at each time step. The constant ζ is equal to one at the start of the attenuating layer (i.e., within the interior where the layer starts and is tapered to a smaller value (e.g. $\zeta_{min} = 0.97$) at the edge of the grid. The MATLAB module which was written for defining these layers, uses a tapering function of the form

$$\zeta(i) = (1 - \zeta_{min})\left[\frac{1 + \cos(\frac{i\pi}{N})}{2}\right]^p + \zeta_{min}; \quad i = 1, ..., N. \tag{16}$$

This type of approach, in conjunction with radiating boundary conditions was used by Fricke[1]. In practice, when using Eq.(16), we used p=2 or p=0.4 and N= 20 or 40 points. In Fig.5 we show the attenuating function of Eq.(16) (with $\zeta_{min} = 0.97$) for N=40 and p=2 (solid line) and p=0.4 (dashed line). The two curves are quite different in character. The $p = 2$ curve has its largest slope in the middle of the transition zone whereas the $p = 0.4$ curve is gradually decaying for much of the curve and then has a large (infinite at the end point) slope at the end. We found that for modelling a point source the $p = 0.4$ curve worked well; however, in general, one must often experiment with the absorbing boundary in order to ensure that the FD solutions are sufficiently free of spurious boundary reflections.

For the FD code of this report, one can use either of the attenuating mechanisms described above or both. For the computations of this report we used only the second technique.

2.4 Specification of incident field

In our implementation of the FD code we use point excitations at grid points to generate incident fields. We consider below some of the details of modelling a point source which lies within the boundaries of the numerical grid. Second, we discuss the generation of an incident field from a distant source by using an array of point sources.

Interior point source

The basic equations of elastic propagation (ignoring any additional visco-elastic terms) can be written as

$$v_{x,t} = \frac{1}{\rho}\left(\frac{\partial \sigma_{xx}}{\partial x} + \frac{\partial \sigma_{xz}}{\partial z}\right) \tag{17}$$

$$v_{z,t} = \frac{1}{\rho}\left(\frac{\partial \sigma_{xz}}{\partial x} + \frac{\partial \sigma_{zz}}{\partial z}\right) \tag{18}$$

$$\sigma_{xx,t} = (\lambda + 2\mu)\frac{\partial v_x}{\partial x} + \lambda\frac{\partial v_z}{\partial z} \tag{19}$$

$$\sigma_{zz,t} = (\lambda + 2\mu)\frac{\partial v_z}{\partial z} + \lambda\frac{\partial v_x}{\partial x} \tag{20}$$

$$\sigma_{xz,t} = \mu\left(\frac{\partial v_x}{\partial z} + \frac{\partial v_z}{\partial x}\right). \tag{21}$$

Let us consider, in an acoustic medium, a point source located at $x = x_s$ (discrete grid point i_s) and $z = z_s$ (discrete grid point j_s) which emits a signal $S(t)$. Since the

medium is acoustic, the terms μ and σ_{xz} can be set to zero in the above equations. Also, $\sigma_{xx} = \sigma_{zz} \equiv \sigma$. Equation(20) can now be written as

$$\sigma_t = \lambda \frac{\partial v_x}{\partial x} + \lambda \frac{\partial v_z}{\partial z} + S(t)\delta(x - x_s)\delta(z - z_s). \tag{22}$$

Differentiating Eq.(22) with respect to time and utilizing Eqs.(17) and (18) we obtain

$$\frac{\partial^2}{\partial t^2}\sigma = \frac{1}{\rho}\lambda\left(\frac{\partial^2 \sigma}{\partial x^2} + \frac{\partial^2 \sigma}{\partial z^2}\right) + \frac{\partial S(t)}{\partial t}\delta(x - x_s)\delta(z - z_s) \tag{23}$$

or

$$\frac{\partial^2 \sigma}{\partial t^2} = c^2\nabla^2\sigma + S_t(t)\delta(x - x_s)\delta(z - z_s). \tag{24}$$

In the discretized version of Eq.(20) the source term is implemented using the equation,

$$\sigma_{xx}(i_s, j_s) \;\; = \;\; \sigma_{xx}(i_s, j_s) + \frac{S(t)(\Delta t)}{\Delta x \Delta z} \tag{25}$$

$$\sigma_{zz}(i_s, j_s) \;\; = \;\; \sigma_{zz}(i_s, j_s) + \frac{S(t)(\Delta t)}{\Delta x \Delta z}. \tag{26}$$

The normalization with respect to Δt is due to the time-discretization of Eqs.(19) and (20); the spatial normalization is chosen so that the source appears as a spatial delta-function with respect to discrete integration [14]. From Eq.(24) it can be seen, that in order to compare the FD solutions with analytical solutions of the acoustic wave equation, it is necessary to use the time-derivative of the source function $S(t)$ as the source function in the analytical solution.

An incident field from a distant source

Because it is necessary to use 10-20 grid points *per* wavelength in the FD modelling, the FD grid corresponds to relatively small physical dimensions for higher frequencies. However, for many problems of interest the source may be so far away from the scattering object or surface, that it is not feasible to include the source point within the computational grid. If the waveguide between the source and the scattering region is sufficiently simple, it may be possible to analytically compute the incident field at the edges of a numerical grid. From the integral relations of the Gauss's divergence theorem [15] we can use these boundary values to excite the FD code and propagate the incident field within the grid. This type of approach has been used previously by authors in electromagnetic modelling (see for example, [16] where an approach very similar to that considered in this report is used). We now present some details of our particular implementation. We consider the case of an acoustic waveguide between the source and scattering region. From Gauss's

Divergence Theorem, we can express the acoustic pressure field at a single frequency ω as

$$p(\omega) = \int_\zeta (G p_{n'} - G_{n'} p) d\ell \tag{27}$$

where ζ is a bounding rectangle located within the computational grid, G is a waveguide Green's function satisfying the Helmholtz equation

$$\nabla^2 G + \frac{\omega^2}{c^2(z)} G = \delta(x - x')\delta(z - z'), \tag{28}$$

and n' denotes the normal derivative with respect to the coordinates of integration along the boundary. We can interpret the integral of Eq.(27) as the pressure field resulting from a distribution of monopole and dipole sources (Huygen's sources [17]). If the source is distant from the scattering region, then the incident field will look like an incident plane-wave (or as we will discuss a generalized plane-wave for a two halfspace medium) in the water column and this plane-wave will have an associated angle of incidence. We define the numerical grid so that one of its edges is normal to the angle of incidence of the plane-wave (Fig. 6) and is internal to the absorbing boundary layer of the grid. We consider Eq.(27) only along this line and ignore the other boundaries' contributions to the incident field. There are different ways of implementing Eq.(27). We can consider a line of appropriately weighted discrete monopole point sources along the boundary. The FD solution for this array of sources effectively performs the integration with respect to the Green's function (a convolution in the time domain). Because of the symmetrical field produced by these monopole sources, $G_{x'}$ is zero along the line and we only have the first term in the integral of Eq.(27). Alternatively, we could simulate a series of dipole sources by placing a sequence of (+) and (-) monopoles one grid point on either side of the bounding edge. In this case only the second term of the integral is required. A simpler method to implement a dipole is to add a spatial delta function (weighted by the incident pressure field normalized by density) to the equation, Eq.(17), for v_x. For all these boundary implementations, the sources produce a field which propagates outwards in both directions. Thus not only the incident field is produced, but also, a field incident on the grid boundary. If, however, the attenuating layer is working well, this field will not reenter the grid. If Eq.(27) is implemented using both the monopoles and dipoles then we can produce only the incident field. The approach implemented in the FD code was to excite the equation for $v_x(z)$ along the line $x = x_{inc}$ with $P(x_{inc}, z, t)/\rho(z)$.

At this point our discussion has been general in terms of form of the incident field; however, we have numerically implemented the case where the incident pressure field is a plane wave with an angle of incidence θ_i in a two halfspace environment. Then the incident field consists of the direct wavefield

$$P^D(x, z, t) = Real\left\{ \int_0^\infty \tilde{S}(\omega) exp\left[i\omega(t - (\frac{x}{c_1}cos(\theta_i) - \frac{z}{c_1}sin(\theta_i))) \right] d\omega \right\}, \tag{29}$$

the reflected wavefield

$$P^R(x,z,t) = Real\left\{\int_0^\infty \tilde{S}(\omega)R(\theta_i,\omega)exp\left[i\omega(t - (\frac{x}{c_1}cos(\theta_i) + \frac{z}{c_1}sin(\theta_i))\right]d\omega\right\}, \quad (30)$$

and a transmitted field,

$$P^T(x,z,t) = Real\left\{\int_0^\infty \tilde{S}(\omega)T(\theta_i,\omega)exp\left[i\omega(t - (\frac{x}{c_2}cos(\theta_t) - \frac{z}{c_2}sin(\theta_t))\right]d\omega\right\}, \quad (31)$$

where

$$R(\theta_i,\omega) = \frac{\rho_2 c_2 sin(\theta_i) - \rho_1\sqrt{c_1^2 - c_2^2 cos^2(\theta_i)}}{\rho_2 c_2 sin(\theta_i) + \rho_1\sqrt{c_1^2 - c_2^2 cos^2(\theta_i)}}, \quad (32)$$

$$T(\theta_i,\omega) = \frac{2\rho_2 c_2 sin(\theta_i)}{\rho_2 c_2 sin(\theta_i) + \rho_1\sqrt{c_1^2 - c_2^2 cos^2(\theta_i)}}, \quad (33)$$

and $\tilde{S}(\omega)$ is the Fourier Tranform of the source function. The factor $\sqrt{c_1^2 - c_2^2 cos^2(\theta_i)}$ is imaginary for θ_i less than the critical angle, in which case the reflection and transmission coefficients are complex. This means that in the time domain the reflected and transmitted pulses are combinations of the source pulse shape and its Hilbert Transform [18].
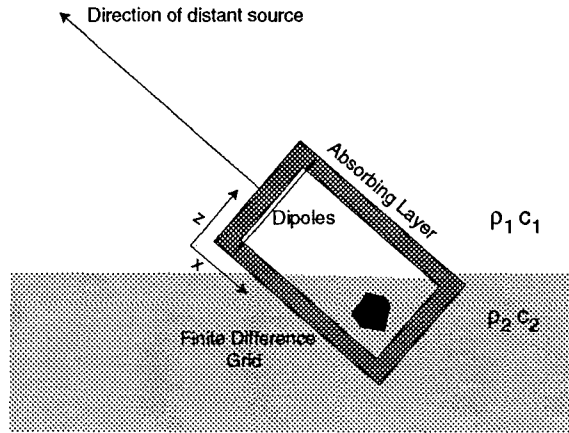

Figure 6: *Schematic diagram of orientation of Finite Difference grid with respect to a distant source*

3

Numerical Examples

In this section we first show the numerical results obtained from the finite difference modelling of propagation and scattering problems, for which we can also compute analytical solutions. In particular, we consider the propagation of an acoustic wavefield from a point source in non-attenuating and attenuating media. We then consider the propagation of a shear plane-wave in an attenuating medium. Finally, for the benchmark cases, we consider the scattering of a compressional plane-wave by solid, thick-shelled, and thin-shelled aluminum cylinders. The shelled cylinders are filled with water. The analytical solutions in this case are computed by solving in the frequency domain a sequence of elastic cylinder scattering problems and then constructing the time-domain pulse by Fourier synthesis.

After these benchmark cases, we consider a buried solid aluminum cylinder and consider a generalized (i.e., consisting of direct, reflected, and transmitted components) plane-wave incident upon this object. We consider the cases of the direct wave in the water column having pre-critical and post-critical angles of incidence. For the case of an evanescent transmitted wave, we examine the effect of a rough interface. Finally we use the FD method to compute the backscattered field from a cylinder at an array of receivers in the water column and then time-reverse this field and use it as the "incident" excitation field. The resulting backpropagated field in the water column focuses at the sources of scattering.

The numerical code was run in Fortran on a DEC-3000 Alpha workstation. A computation with a 440 × 440 grid and 12000 time steps required 128 minutes of CPU time. In the following examples, the absolute levels of the computed pressure fields have often been scaled for plotting purposes.

3.1   Computations in a homogeneous medium

First we consider a point source in a homogeneous acoustic space. We consider the source function in Eq.(22) to be the time derivative of a Gaussian pulse, [1],

$$S(t) = -2\sigma(t - t_s)e^{-\sigma(t-t_s)^2} \tag{34}$$

where

$$\sigma = \left(\frac{\omega_0}{2}\right)^2, \tag{35}$$

$$t_s = \frac{4\pi}{\omega_0} \tag{36}$$

and ω_0 is the central angular frequency which we take to be 1500 Hz. We take the sound speed to be $c_0 = 1500$ m/s. Thus the reference wavelength for this example is 1m. We do our computations with $\Delta x = 0.05$ m or $\lambda/20$. From our previous discussion of stability limits, we must use a time step Δt such that

$$\Delta t < .606\frac{\Delta x}{1500} \approx 2 \times 10^{-5}s. \tag{37}$$

We use $\Delta t = 10^{-5}sec$ which is approximately half the stability limit. We consider a numerical grid which is 300×300 in dimension. We use 40 points for the absorbing boundary layer. We construct this absorbing layer using the second absorbing mechanism described in subsection 2.4. We found that using a fractional power $p = 0.4$ in Eq.(16) with $\zeta = 0.95$ worked well. In Fig.7 below, we show the FD signal as a
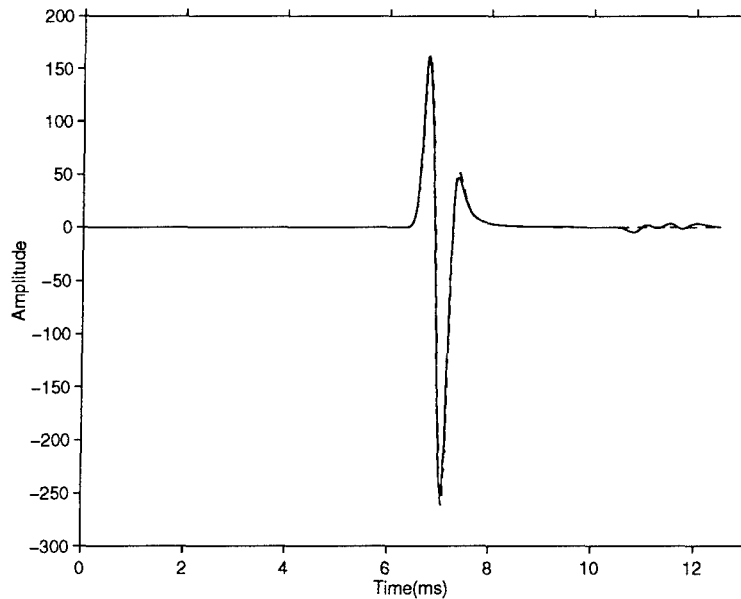

Figure 7: *Finite difference (solid line) and analytical (dashed line) pulse shapes for receiver at 8.5 wavelengths from the source*

solid line along with the analytical solution of Eq.(24) (dashed line) for a source at $(i,j) = (70, 150)$ and a receiver at $(i,j) = (240, 150)$ (where (i,j) denote the discrete indices for the (x, z) coordinates). The agreement is excellent between the computed and analytical solutions with only small artifacts due to the boundaries in the tail of the signal.

We now consider the same geometry as above, but for a medium with $Q = 20$. In Figure 8a we show the comparison between the FD computed pulse and an "analytically" computed pulse. The analytical solution used Fourier synthesis and a Q/dispersion relation of the form of Eqs.(14) and (15) with the parameters which were used for the computation of the curve of Fig. 3. The agreement is excellent. In Fig. 8b we show a comparison between the FD pulse and the analytical solution if no frequency dispersion is used; i.e., we fixed the phase velocity at $c = 1500$ m/s for all frequencies and simply added an imaginary part to the sound speed to produce the required attenuation. This procedure is the usual approach in frequency domain modelling. The agreement between the two pulses is no longer so good. The amplitudes of the two pulses are similar but the shape of the pulses are noticeably different. We have used a large attenuating factor in this example; the differences between the curves in Fig. 8b would be less for smaller attenuation. Finally in Fig. 8c we show the analytical pulse computed for a $Q=1000$ (no attenuation). In this case the pulse is too large in amplitude, illustrating the importance of attenuation in this example.
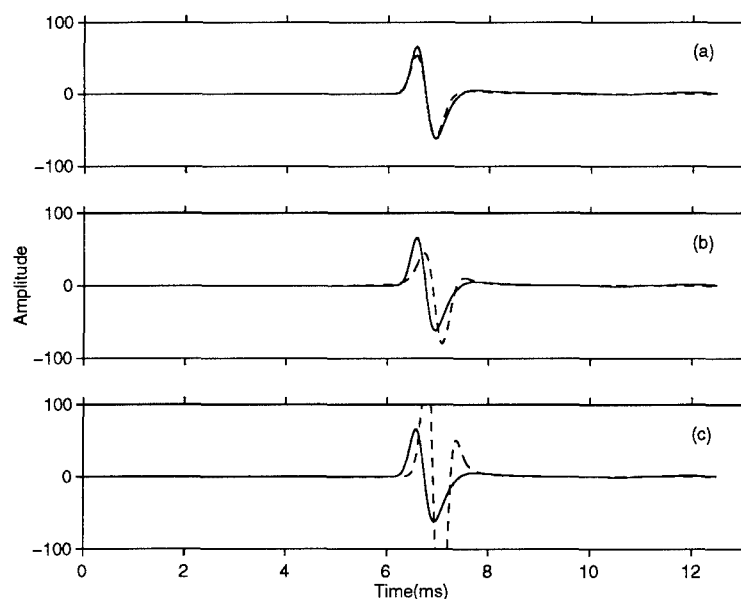

Figure 8: *Finite difference (solid line) and analytical pulse shapes (dashed line) for $Q = 20$ for (a) analytical solution computed accounting for frequency dispersion (b) attenuation model with a fixed phase velocity of $1500m/s$ (c) using $Q=1000$*

We now consider an example with a non-zero shear speed. In particular we excite the equation for v_z with an array of point sources along the line $x = 70$. This arrangement should excite a shear plane-wave. However, due to the fact that there is a finite, discrete aperture of sources the synthesis of the plane-wave is not exact and other energy, some of it compressional in nature, is excited. We use an absorbing

layer of 40 points in this case, with $\zeta = 0.96$ and $p = 2$. To reduce the amount of spurious energy produced by the edge effects of a finite aperture of sources, we weight the source terms by a cosine taper away from the centre of the grid. The source time history is the same as for the previous example. However, we now take the compressional sound speed to be $c_p = 3000m/s$ and the shear speed $c_s = 1500m/s$. Because of the high compressional sound speed we use $\Delta t = 10^{-5}/2$. We define the Q factor for the compressional waves to be $Q_p \equiv 1000$ throughout the grid and the Q factor for the shear waves $Q_s \equiv 20$. If the FD code is correctly modelling the elastic and attenuation properties of the medium, the wave propagation for this example should be well-modelled as a shear plane wave attenuated by a Q value of 20. In Fig.9 we show the pulse (we plot v_z) at the centre of the grid at $x = 240$ as computed by the FD code (solid line) and analytically (dashed) for an attenuated shear plane wave. The agreement between the two curves is good. There is a small amount of spurious energy, some of which is compressional (note that any compressional energy is much less attenuated than the true shear energy as we have used $Q_p = 1000$ for this example). It is interesting to note that for this example, the Green's function which we use in the computation of the analytic solution is of the form

$$\frac{exp(i\omega/c|x - x_s|)}{2i\omega/c} \tag{38}$$

whereas in the point source example the Green's function was of the form

$$\frac{i}{4}H_0^1(\omega/c\sqrt{(x - x_s)^2 + (z - z_s)^2}) \tag{39}$$

3.2 Computations for an elastic cylinder surrounded by an homogeneous fluid

We now consider an aluminum cylinder of radius 1 m located in an homogeneous compressional space with $c_p = 1500m/s$ and $\rho = 1000kg/m^3$. For the aluminum cylinder we use the parameters $c_p = 6380m/s$, $c_s = 3136m/s$ and $\rho = 2172kg/m^3$. Because of the large velocities within the cylinder it is necessary to take small time steps. We used $\Delta x = 0.025m$ (or 40 points per wavelength) and $\Delta t = 0.01/8ms$ in our computations with a 400×400 grid. The cylinder is located at the centre of the numerical grid. A normal-incidence plane-wave was excited by applying point source functions to σ_{xx} and σ_{zz} along the line $x = 1.5m$ with the time-history of a time-differentiated gaussian. In order to reduce edge effects we tapered the incident plane-wave by a cosine-weighting for the first and last 100 points of the grid. Figure 10 shows a comparison of the FD time series with the time series computed using Fourier synthesis and the harmonic Fourier-Bessel series for the scattered field from an infinite elastic cylinder. The series were computed for receivers 3.5 m from the centre of the cylinder at angles of $0°$, $90°$, $270°$ and $180°$ with respect to the cylinder
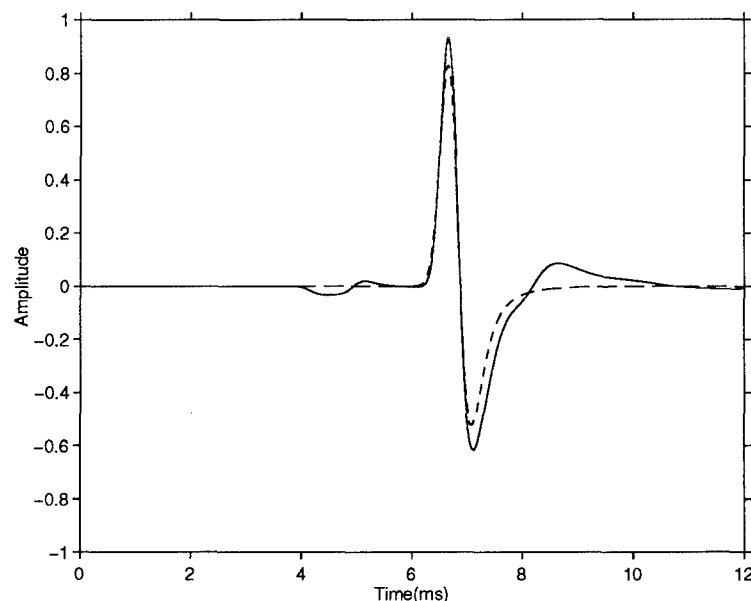
Figure 9: *Finite difference (solid line) and analytical pulse shapes (dashed line) for a shear plane-wave with Q = 20*

centre. From symmetry, the time series for $\theta = 90°$ and $270°$ should be identical. However, this is not true in practice due to the staggered grid formulation of the RBS FD code. Although the FD solution is initially symmetrical, the symmetry of the field is not sustained over time. The FD and analytical amplitudes of the incident wave do not agree well for the receivers at $90°$ and $270°$ because the tapering of the plane-wave is significant at these locations. The scattered fields, however, are caused by the scattering of the incident field at the cylinder and these amplitudes are correctly modelled.

We now repeat the above numerical experiment with a shelled cylinder. We consider an aluminum shell 0.5 m thick (or 20 grid points) with the interior of the cylinder filled with water. The comparison with the analytic solution is shown in Fig. 11. The agreement between the numerical and analytic solutions is good.

By varying the shell thickness, we found that good agreement between computed and analytical results were obtained down to and including shell thicknesses of 3 grid points corresponding to a relative shell thickness of 7.5%; by decreasing the spatial discretization size we should be able to decrease this ratio. The comparison between the FD curves and the analytical curves are shown in Fig. 12. In Fig. 13 we show a snapshot of the pressure field for the thick shelled cylinder 4 ms into the computation. The plane-wave can be seen passing by the exterior of the cylinder. A faster wavefront has already passed through the cylinder and the backscattered wavefront is visible at the front of the cylinder.
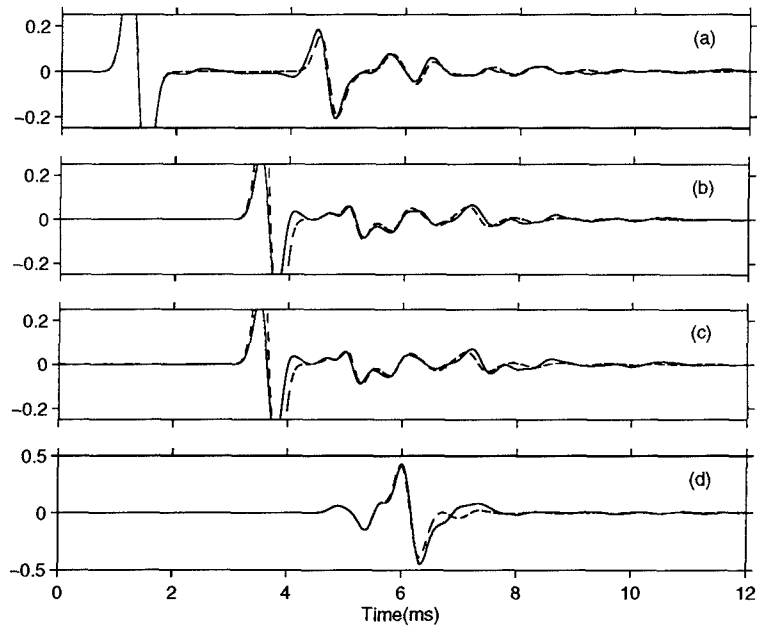
Figure 10: *Finite difference (solid line) and analytical time series (dashed line) for receivers at (a) 0° (backscatter) (b) 90° (c) 270° and (d) 180° (forward direction) for an infinite elastic (aluminum) cylinder*
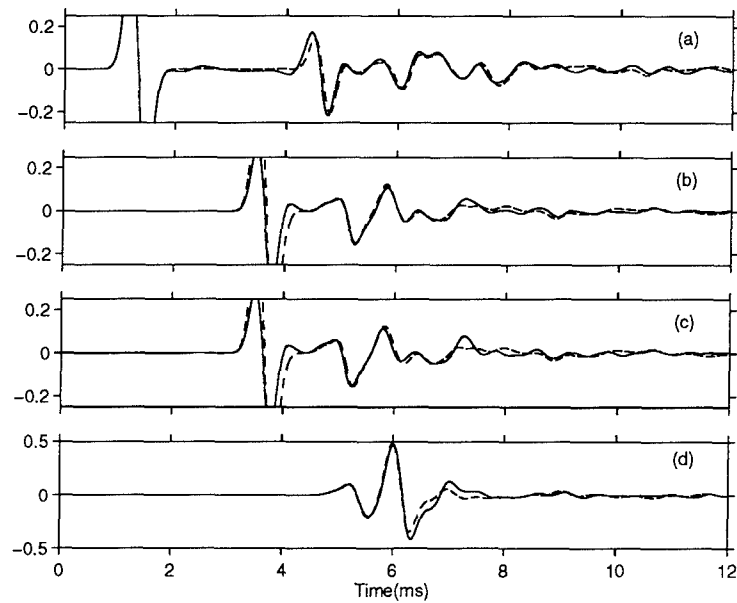

Figure 11: *Finite difference (solid line) and analytical time series (dashed line) for receivers at (a) 0° (backscatter) (b) 90° (c) 270° and (d) 180° (forward direction) for thick-shelled (20 grid points) cylinder filled with water*
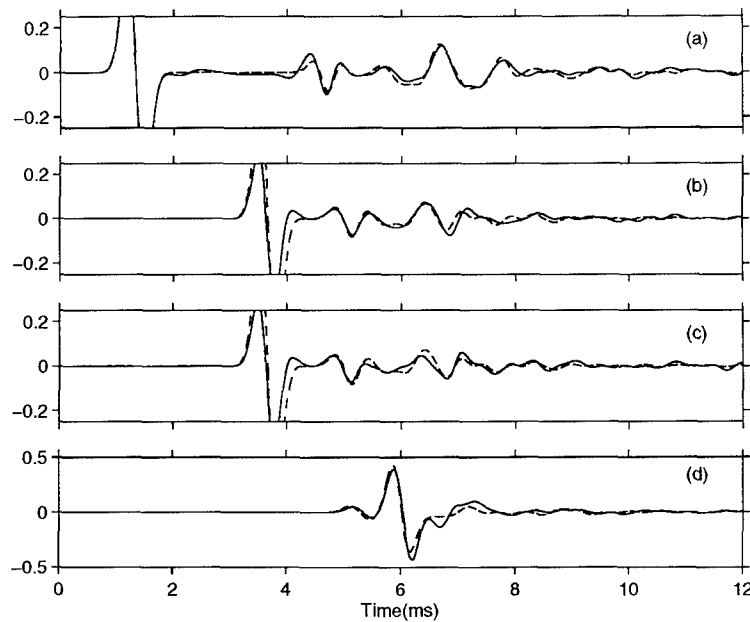
Figure 12: *Finite difference (solid line) and analytical time series (dashed line) for receivers at (a) 0° (backscatter) (b) 90° (c) 270° and (d) 180° (forward direction) for thin-shelled (3 grid points) cylinder filled with water*

3.3 Scattering of a generalized plane-wave by a buried cylinder

We can simulate an incident acoustic or elastic wavefield by exciting monopole and dipole sources along the boundaries of the grid. In these examples, we only use dipole excitation. We excite the particle velocity v_x by $p^{inc}/\rho(z)$. This means that the correct field propagates into our grid, but also a mirror-image field propagates to the left where it is attenuated by the absorbing layer of our grid. By exciting the normal stress by p_x^{inc}, it should be possible to eliminate the left-going field.

In the examples which follow, we will consider a fluid half-space with sound speed 1500 m/s and $\rho = 1000kg/m^3$ overlying another fluid space with sound speed 1700 m/s and $\rho = 1500kg/m^3$. The critical angle for these parameters is $\theta_c = 28.07°$ (measured from the horizontal). We first consider the case of the angle of incidence $\theta = 30°$. We consider our grid rotated so that the boundary of excitation is parallel to the incident direct wave and as a result the fluid/fluid interface has a slope of 30°. The advantage of this approach is that one obtains a maximum aperture of sources, using a single boundary, to simulate an incident field. The disadvantages are (1) that the interface is sloping upwards to the right of the incident excitation line and it is difficult to know how to model the bathymetry to the left of the incident line in order to avoid diffraction effects at the intersection of the interface boundary and the vertical array of excitation sources; (2) because the interface is sloping we are,
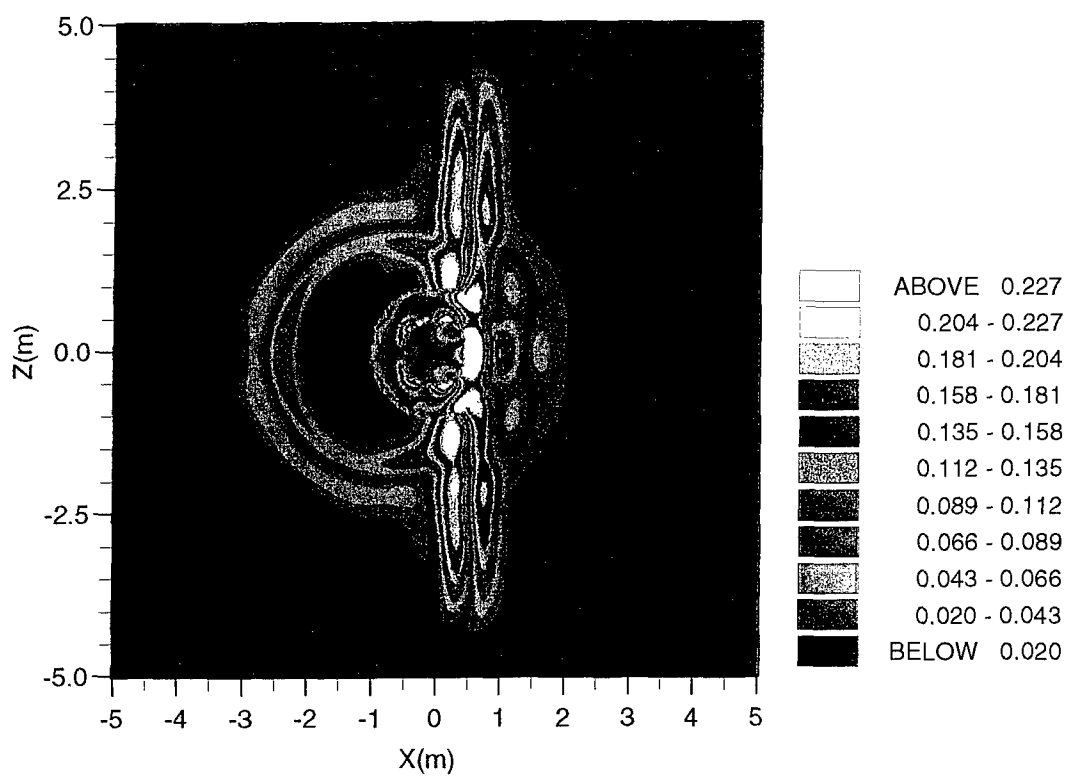
Figure 13: *Snapshot of pressure field at 4 ms for thick-shelled aluminum cylinder filled with water*

in fact, approximating it with a staircase in the FD approximation and these small stairsteps cause small diffractions. However, we find that despite these problems the incoming incident field is well-behaved. In Fig. 14 we show the incident field (i.e., $p(z,t)/\rho(z)$) which is used to excite v_x. The vertical axis is depth and the horizontal axis is time. The direct pulse appears vertically oriented. As can be seen there is significant energy transmitted into the bottom. For the FD computations of this set of examples, we used a 440×440 grid with 60 points in the absorbing layer ($\zeta_{min} = 0.96$, $p = 2$). The equations for v_x were excited at the line $x_{inc} = 63$. In Fig. 15 we show a time snapshot of the pressure field after the plane wave in the bottom has interacted with the buried aluminum cylinder. There is a substantial reflected field from the cylinder. Only the field in the square region interior to the absorbing boundary layers and the line of dipoles is shown.
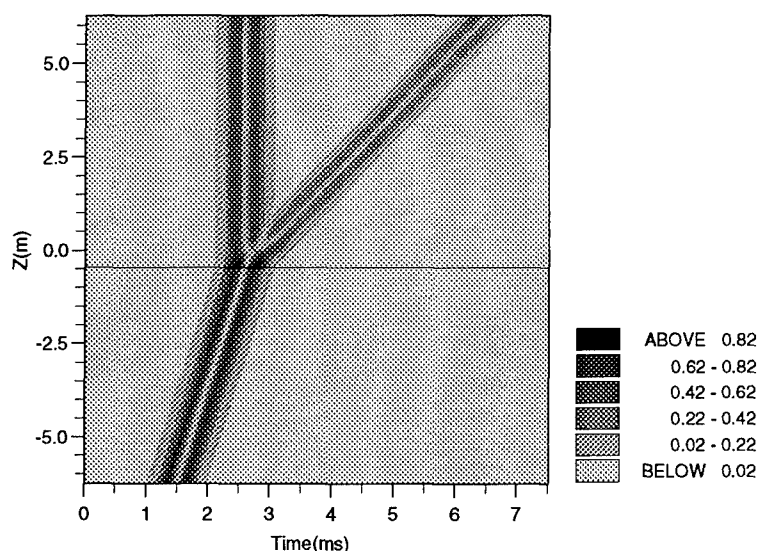

Figure 14: *Incident plane-wave field (absolute value) used to excite vertical array of dipole sources for $\theta = 30°$.*

Next, we consider the case for the angle of incidence of the direct plane-wave in the water column being post-critical, $\theta = 20°$. The incident field used to excite the equation for v_x is shown in Fig. 16.

In this case the transmitted field is evanescent and the reflected pulse is a temporal combination of the direct pulse and its Hilbert Transform. There is a region of high intensity near the interface where the incident and reflected waves interfere with each other. In Figs. 17, 18, and 19 we show a single time snapshot for the wavefields generated in the case of a buried solid aluminum cylinder, for a rough interface with no cylinder, and the same rough interface with a buried cylinder. In Fig. 17 we see that the incident field of Fig. 16 has propagated into the grid. The exponential tail of the transmitted wave just touches the cylinder. There is a small amount of energy
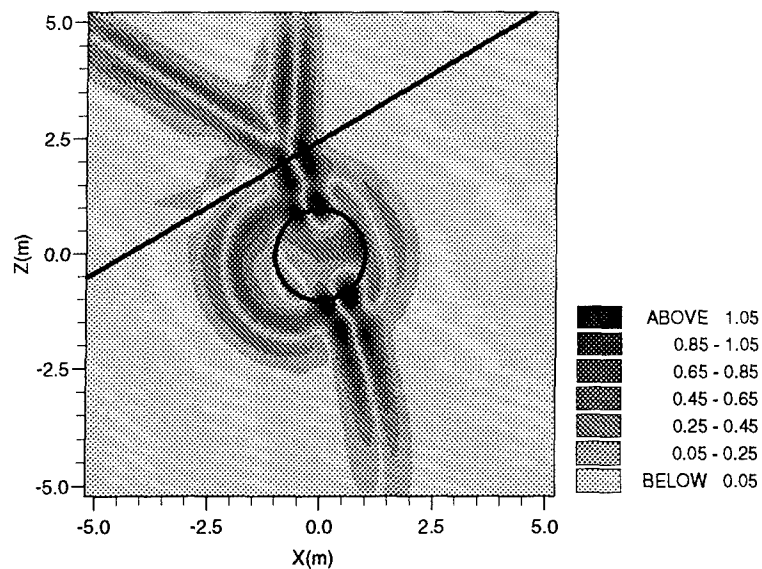
Figure 15: *Time snapshot of pressure field (absolute value) resulting from interaction of transmitted wavefield with cylinder*
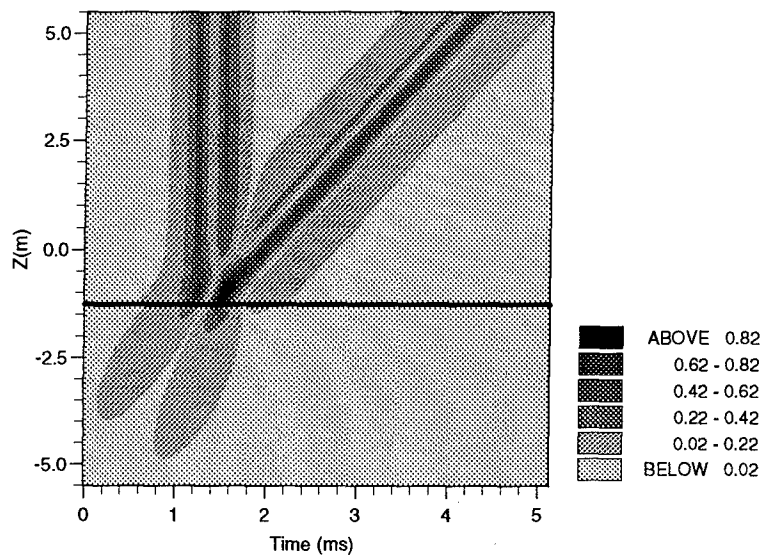

Figure 16: *Incident plane-wave field (absolute value) used to excite vertical array of dipole sources for $\theta = 20°$.*
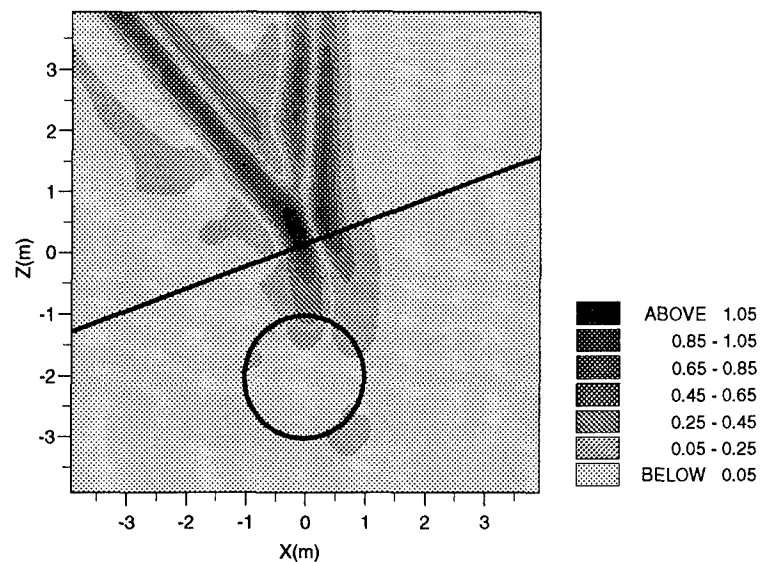
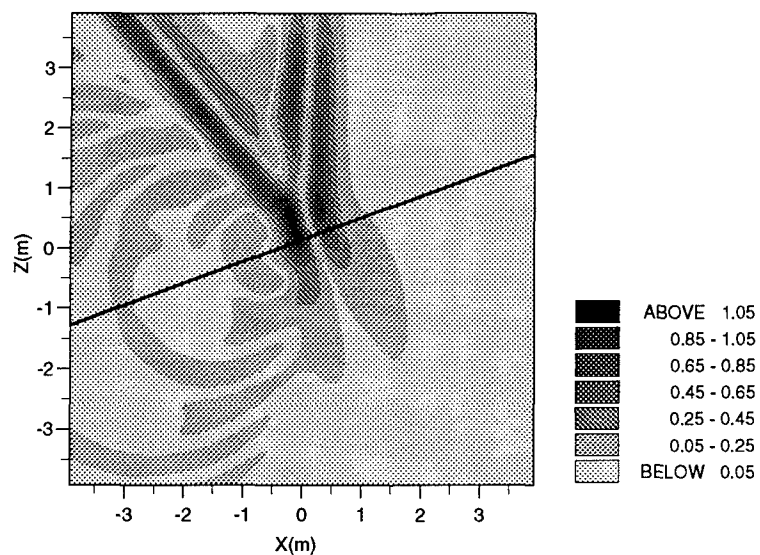Figure 17: *Propagating plane-wave field (absolute value) with buried aluminum cylinder*

Figure 18: *Propagating plane-wave field (absolute value) with rough interface*
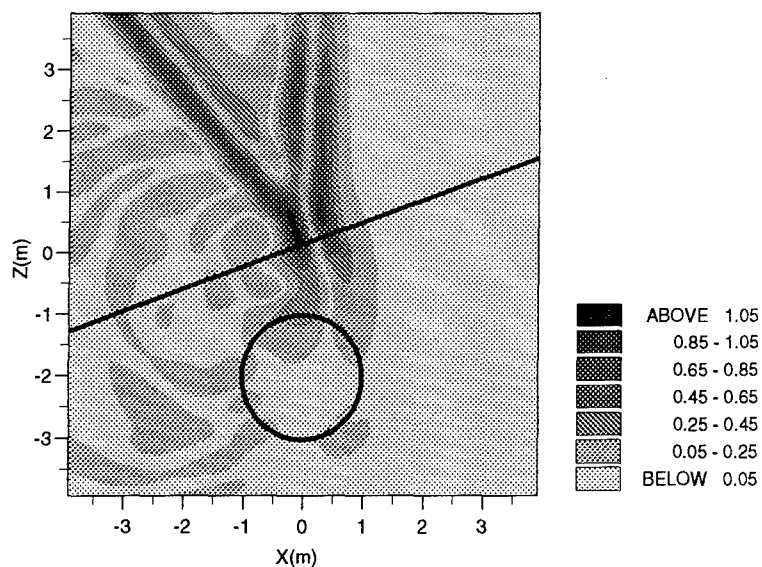
Figure 19: *Propagating plane-wave field (absolute value) with rough interface and buried aluminum cylinder*
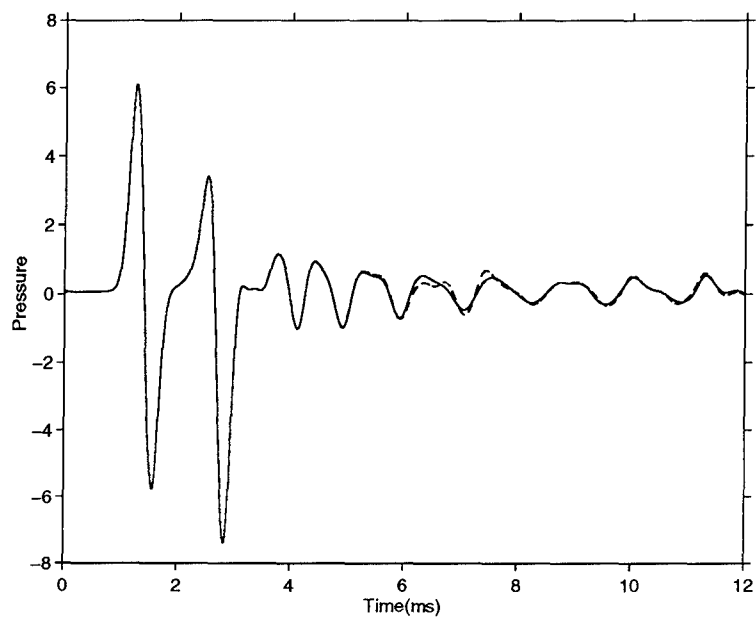

Figure 20: *Time series at a receiver located 3.25 m above interface at incident array when there is no cylinder in the bottom (solid line) and when there is a cylinder in the bottom (dashed line)*

following the incident wavefield which was probably incorrectly created during the generation of the incident wavefield from the dipoles. This can sometimes be an annoyance when generating incident post-critical wavefields; it is not surprising that the use of a discontinuous (because of the $1/\rho(z)$ normalization), analytic wavefield to excite a discrete numerical grid may cause the excitation of a small amount of spurious energy near the interface. It may be possible to reduce this problem by smoothing the incident wavefield and/or the medium, but we did not do this for these results.

The "rough" interface of Figs. 18 and 19 is generated from the equation

$$j = 170 + (i - 63)\tan(20°) + 10\sin(\frac{2\pi(i - 63)}{40}). \tag{40}$$

Here j is the vertical index and i the horizontal index. There are 40 points per wavelength used in this example so that the peak-to-peak roughness is 1/2 wavelength and the wavelength of the roughness is one wavelength. The rough interface generates backscattered energy and also transmits energy into the bottom (Fig. 18). This energy can significantly interact with the cylinder (Fig. 19) - however, the differences between Figs. 18 and 19 in the water column are very slight. This is emphasized in Fig. 20 where we show the received timeseries for a receiver 3.25 m above the interface at the horizontal location of the array of Huygen's sources for the case of no cylinder in the bottom (solid line) and a cylinder in the bottom (dashed line). The two curves are almost indistinguishable. There is, however, a small but noticeable difference between the two curves in the 6-8 ms interval. Another interesting feature of these two curves is the the appearance of a definite frequency of backscatter for this case. This is expected from a perturbation analysis of the rough interface. Following the work of, for example, [19] we expect for our given roughness wavelength that the maximum backscattered field should occur approximately when

$$2\frac{\omega}{1500} = 2\pi\lambda(\text{perturbation}) \tag{41}$$

In our case the perturbation has a wavelength of 1 m so that we find an optimal frequency of approximately 750 Hz or a period of oscillation of 1.3 ms which agrees well with the result of Fig. 20.

3.4   An example of time reversed propagation

As shown above it is straightforward to introduce an incident field into the grid by using an array of monopoles and/or dipoles. Another interesting application of this concept, is to time-reverse [20] the scattered field at the receiving array and propagate it back into the medium. We would expect the field which has been scattered from compact objects to focus back at those same objects.

We consider the same cylinder and medium as the previous example but now the cylinder is only partially buried. A time snapshot of the pressure field is shown in Fig. 21 just after the incident field has encountered the cylinder. In Fig. 22 we
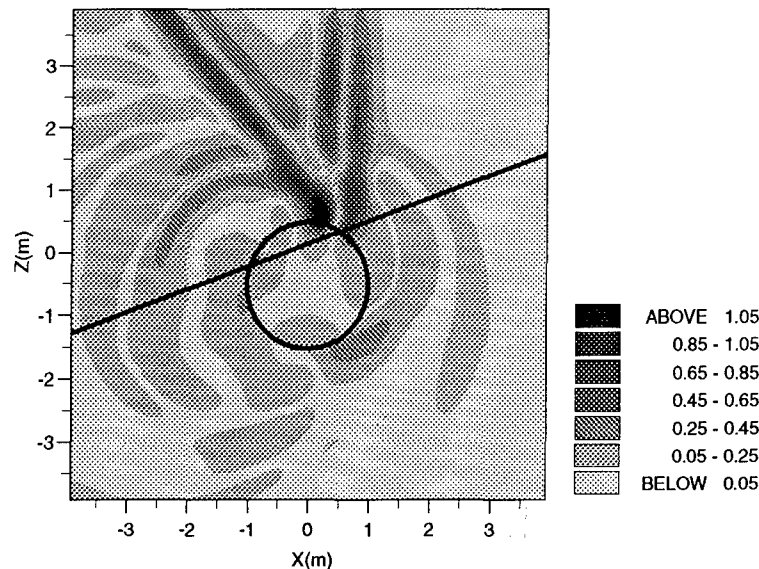

Figure 21: *Plane-wave field incident on partially buried aluminum cylinder*

show the time-reversed pressure field recorded by 210 receivers. The first of these receivers is located in the water just above the interface and the others are located sequentially above it. Starting from the right hand side of the plot, the incident field is evident, then backscatter from the rough interface, and then from 7.0 to 5.5 ms an event associated with backscatter from the cylinder, and then finally backscatter from the rough interface again. The field of Fig. 22 is then used to excite the array of dipoles (just for the positions of the 210 receivers). We stop the time-reversed field just prior to the time that the original incident field is present in the time series. In this numerical experiment of time-reversed propagation, we suppose that we do not know what created the scattered field. Hence although the cylinder was used in the FD modelling to produce the scattered field of Fig. 22, it is not included in the model for the backpropagation of this energy. Instead, only a two halfspace medium is used in the modelling of the backpropagated scattered field. In Figs. 23 and 24 we show 2 time snapshots of the resulting field as it propagates back into the grid. Figure 23 shows the field scattered from the cylinder just starting to focus and Fig. 24 shows the field close to the time of maximum focussing; the focus is along the side where the original specular reflection occurred. For this example, our recording aperture did not sufficiently surround the scatterer and the frequency of the source was not high enough to obtain a good definition of the scattering object; nevertheless, the backpropagated field did focus at the correct location, corresponding to the area of specular reflection from the object.
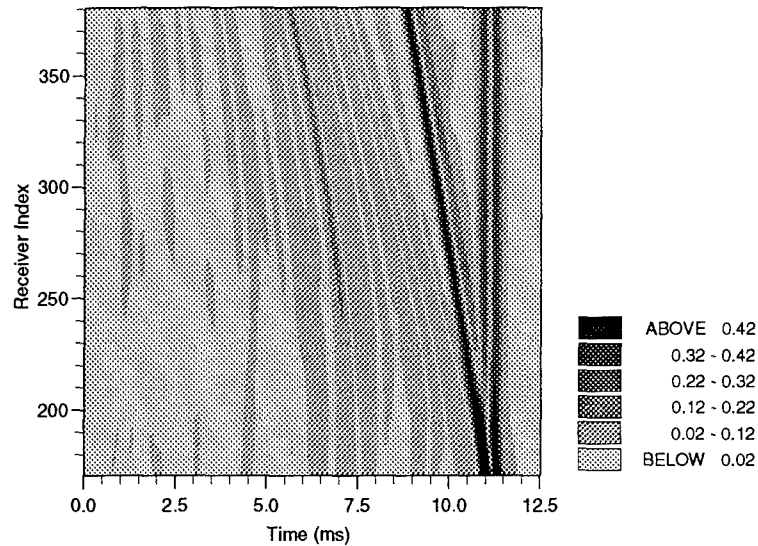
Figure 22: *The time history of the time-reversed pressure field (absolute value) as recorded along a vertical array of receivers located at the line of incidence*
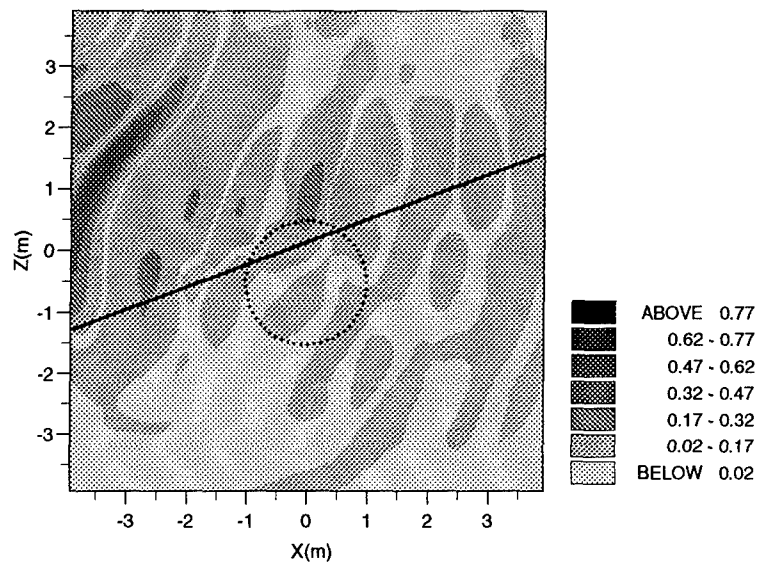

Figure 23: *Back-propagated field (absolute value) as scattered field is just starting to focus; the cylinder is not used in the modelling*
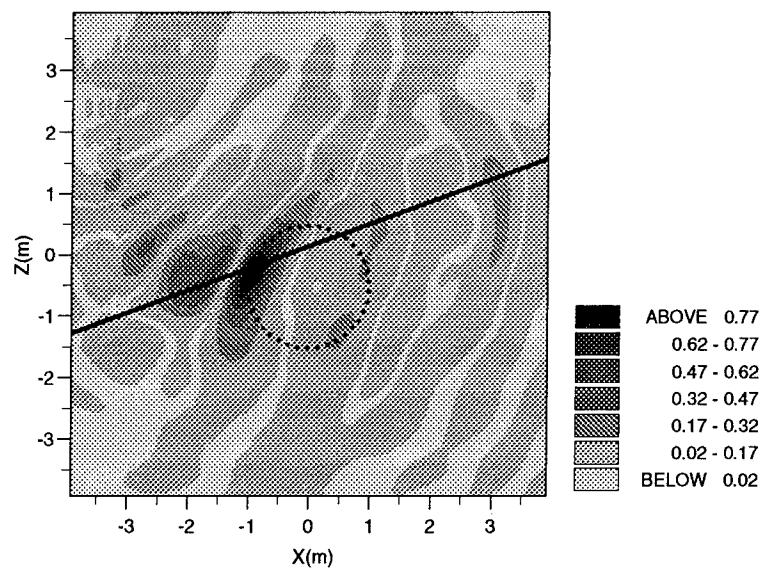
Figure 24: *Back-propagated field (absolute value) near the time of maximum focusing; the cylinder is not used in the modelling*

4

Summary

We have described some of the theory underlying a visco-elastic Finite Difference code (in particular, the RBS FD code). We compared the FD computations with a suite of analytical cases for both homogeneous propagation and scattering and found that the FD results were in good agreement with the analytical results. The attenuation properties of the FD code are in good agreement with analytical computations if one uses a realistic frequency dipersion relation in the analytical modelling. We did computations of scattering from aluminum cylinders, which have a very high velocity/density contrast with the surrounding fluid and obtained good agreement with analytical computations for the 4 quadrants of scattering, although the results were best for the backscatter direction. We consider aluminum shells of varying thickness and found that we obtained good results for shells only 3 grid points thick.

We then showed how we could introduce an incident field into the grid by exciting an array of dipoles. We used this concept to introduce a generalized plane-wave, corresponding to a two half-space medium into the grid. In particular we considered an incident wave for which the wavefield in the bottom half-space was evanescent and considered the scattering by a buried aluminum cylinder. We then repeated the computations for a rough interface. For this particular example, the rough interface introduced more energy into the bottom but the signal received in the water column was dominated by the backscatter from the rough interface. Reflected energy from the cylinder was just observable in the backscattered signal. Finally, we showed that with the incident-field formulation of this code, one can easily back-propagate scattered fields and focus this energy into areas of high reflectivity.

5

Acknowledgements

References

[1] J.Robert Fricke. *Acoustic Scattering from Elastic Ice: A Finite Difference Solution*. PhD thesis, Woods Hole Oceanographic Institution, Massachussetts Institute of Technology, June 1991.

[2] J.Robert Fricke. Acoustic scattering from elemental ice features: Numerical modeling results. *Journal of the Acoustical Society of America*, 93:1784–1796, 1993.

[3] Martin E. Dougherty and Ralph A. Stephen. Geoacoustic scattering from seafloor features in the ROSE area. *Journal of the Acoustical Society of America*, 82:238–256, 1987.

[4] Jean Virieux. P-SV wave propagation in heterogeneous media: Velocity-stress finite-difference method. *Geophysics*, 51:889–901, April 1986.

[5] Johan O.A. Robertsson, Joakim O. Blanch and William W. Symes. Viscoelastic finite-difference modeling. *Geophysics*, 59:1444–1456, September 1994.

[6] Johan O.A. Robertsson, Joakim O. Blanch and William W. Symes. Modeling of a constant Q: Methodology and algorithm for an efficient and optimally inexpensive viscoelastic technique. *Geophysics*, 60:176–184, 1994.

[7] *MATLAB High-Performance Numeric Computation and Visualization Software Reference Guide.*

[8] José M. Carcione, Dan Kosloff, and Ronnie Kosloff. Wave propagation simulation in a linear viscoacoustic medium. *Geophysical Journal*, 93:393–401, 1988.

[9] Johan O.A. Robertsson and Alan Levander. A numerical study of seafloor scattering. *Journal of the Acoustical Society of America*, 97:3532–3546, 1995.

[10] Keiiti Aki and Paul G. Richards. *Quantitative Seismology: Theory and Methods, Vol.I.* W.H. Freeman and Company, 1980.

[11] Walter I. Futterman. Dispersive body waves. *Journal of Geophysical Research*, 67:5279–5291, 1962.

[12] Paul C. Wuenschel. Dispersive body waves - an experimental study. *Geophysics*, 30:539–551, 1965.

[13] R.W. Clayton and B. Enquist. Absorbing boundary conditions for wave-equation migration. *Geophysics*, 45:895–904, 1980.

[14] John A. Fawcett. Two dimensional velocity inversion of the acoustic wave equation. *Wave Motion*, 7:503–513, 1985.

[15] Julius A. Stratton. *Electromagnetic Theory*. McGraw-Hill Book Company, 1941.

[16] P. Bill Wong, G.Leonard Tyler, John E. Baron, Eric M. Gurrola, and Richard A. Simpson. A three-wave FDTD approach to surface scattering with applications to remote sensing of geophysical surfaces. *IEEE Transactions on Antennas and Propagation*, 44:504–514, 1996.

[17] C.P.A. Wapenaar and A.J. Berkhout. *Elastic Wave Field extrapolation, Redatuming of single- and multi-component seismic data*. Elsevier Science Publishers, 1989.

[18] L. M. Brekhovskikh and O. A. Godin. *Acoustics of Layered Media I - Plane and Quasi-plane Waves*. Springer-Verlag, 1989.

[19] Brian T.R. Wetton and John A. Fawcett. Scattering from small three-dimensional irregularities in the ocean floor. *Journal of the Acoustical Society of America*, 85:1482–1488, 1989.

[20] Christian Dorme and Mathias Fink. Focusing in transmit-receive mode through inhomogeneous media: The time reversal matched filter approach. *J. Acoust. Soc. Am.*, 98:1155–1162, 1995.

Document Data Sheet

NATO UNCLASSIFIED

Security Classification		Project No.
NATO UNCLASSIFIED		033-3

Document Serial No.	Date of Issue	Total Pages
SR-256	July 1996	40 pp.

Author(s)

Fawcett, J.A. and Grimbergen, J.L.T.

Title

Finite difference modelling of scattering by objects in the seabed.

Abstract

In this report we describe the theory and some implementation issues of a finite difference code used at SACLANT Centre. In particular, we consider the modelling of attenuation and the excitation of a remote incident field by using Huygen's sources. A series of comparisons of finite difference results with analytical results is performed. The report concludes with a series of computations of scattering of a generalized plane wave from a buried cylinder where the transmitted portion of the generalized plane wave is evanescent. An example of time-reversed propagation of a scattered field is also given.

Keywords

Finite difference modelling – attenuation – Huygen's sources

Ministries of Defence		Scientific Committee of National Representatives	
DND Canada	10	SCNR Belgium	1
CHOD Denmark	8	SCNR Canada	1
DGA France	8	SCNR Denmark	1
MOD Germany	15	SCNR Germany	1
HNDGS Greece	12	SCNR Greece	1
MARISTAT Italy	10	SCNR Italy	1
MOD (Navy) Netherlands	12	SCNR Netherlands	2
NDRE Norway	10	SCNR Norway	1
MOD Portugal	5	SCNR Portugal	1
MDN Spain	2	SCNR Spain	1
TDKK and DNHO Turkey	5	SCNR Turkey	1
MOD UK	40	SCNR UK	1
ONR USA	42	SCNR USA	1
		SECGEN Rep. SCNR	2
		NAMILCOM Rep. SCNR	1
NATO Commands and Agencies		French Delegate	1

NATO Commands and Agencies		
NAMILCOM	2
SACLANT	3

National Liaison Officers

CINCEASTLANT/		National Liaison Officers	
COMNAVNORTHWEST	1	NLO Canada	1
CINCIBERLANT	1	NLO Denmark	1
CINCWESTLANT	1	NLO Germany	1
COMASWSTRIKFOR	1	NLO Italy	1
COMMAIREASTLANT	1	NLO Netherlands	1
COMSTRIKFLTANT	1	NLO UK	1
COMSUBACLANT	1	NLO USA	1
SACLANTREPEUR	1		
SACEUR	2		
CINCNORTHWEST	1		
CINCSOUTH	1		
COMEDCENT	1		
COMMARAIRMED	1	**Sub-total**	**228**
COMNAVSOUTH	1		
COMSTRIKFORSOUTH	1	SACLANTCEN	30
COMSUBMED	1		
SHAPE Technical Centre	1	**Total**	**258**
PAT	1		